RSC Advances

PAPER

View Article Online
View Journal | View Issue

Cite this: *RSC Adv.*, 2020, **10**, 38736

Strong electron acceptor additive based spiro-OMeTAD for high-performance and hysteresis-less planar perovskite solar cells†

Shibo Wang, Weihai Sun,* Mingjing Zhang, Huiying Yan, Guoxin Hua, Zhao Li, Ruowei He, Weidong Zeng, Zhang Lan and Jihuai Wu*

Received 24th August 2020
Accepted 14th October 2020

DOI: 10.1039/d0ra07254k

rsc.li/rsc-advances

As the most popular hole-transporting material (HTM), spiro-OMeTAD has been extensively applied in perovskite solar cells (PSCs). Unluckily, the pristine spiro-OMeTAD film has inferior conductivity and hole mobility, thus limiting its potential for application in high-performance PSCs. To ameliorate the electrical characteristics of spiro-OMeTAD, we employ 2,3-dichloro-5,6-dicyano-1,4-benzoquinone (DDQ) as a strong electron acceptor into spiro-OMeTAD in PSCs. The incorporation of DDQ with spiro-OMeTAD not only improves the conductivity and the Fermi energy level, but also reduces the trap states and nonradiative recombination, which accounts for the remarkable enhancement in both the fill factor (FF) and open-circuit voltage (V_{OC}) of PSCs. Consequently, the champion PSC with DDQ doped hole transport layer (HTL) generates a boosted power conversion efficiency (PCE) of 21.16% with an FF of 0.796 and a V_{OC} of 1.16 V. Remarkably, DDQ modified devices exhibit superb device stability, as well as mitigated hysteresis. This study provides a facile and viable strategy for dopant engineering of HTL to realize highly efficient PSCs.

1. Introduction

Organic–inorganic hybrid perovskite solar cells (PSCs) as a type of burgeoning solar technology, have been extensively investigated over the past decade because of their low cost, feasible fabrication procedure and high power conversion efficiency (PCE).[1–6] Since the first breakthrough of the implementation of an organic solid hole-transporting material (HTM) [2,2′,7,7′-tetrakis-(*N*,*N*-di-*p*-methoxyphenylamino)-9,9′-spiro-bifluorene] (spiro-OMeTAD) in PSCs took place, the PCE has experienced unprecedentedly rapid development from beyond 9% (ref. 7 and 8) to a record exceeding 25%.[9]

The hole transport layer (HTL), a crucial constituent of PSCs, is inserted between the perovskite absorber film and the electrode.[10,11] Excellent HTLs can not only offer a route for transporting holes and blocking electrons, but also play as a layer of protection to inhibit oxygen and moisture from deteriorating the perovskite films.[12–14] Among the various HTMs, the state-of-the-art spiro-OMeTAD is intensively applied as the predominant HTM for highly efficient PSCs, due to its appropriate energy level, low glass-transition temperature and superior solution processability.[15–17] However, its fairly low hole mobility and conductivity restrict its commercial application as an HTL for high performance PSCs.[18,19] To overcome this issue, several useful strategies for enhancing electrical conductivity and hole mobility have been proposed, one of which is chemical p-doping.[20] Numerous chemical additives have been introduced as dopants to strikingly improve the conductivity of HTLs in PSCs, such as lithium salts,[21] cobalt(III) salts,[22] ionic liquids,[23] F4-TCNQ[24] and *etc.* Doping lithium bis(trifluoromethanesulfonyl)-imide (Li-TFSI) and 4-*tert*-butyl pyridine (*t*BP)[25] is a widespread treatment for improving the hole density and energy level of HTL. Unluckily, it takes a long time for the efficient oxidation of spiro-OMeTAD by Li-TFSI, which usually needs the oxygen atmosphere, thereby resulting in poor reproducibility and weak stability of PSCs.[26,27] In order to accelerate the oxidation, inorganic chemicals including $FeCl_3$,[28] $SnCl_4$,[29] $KMnO_4$ (ref. 30) and V_2O_5 (ref. 31) have been applied into spiro-OMeTAD solution with *t*BP and Li-TFSI. Unfortunately, the poor solubility of inorganic p-dopants in organic solvents is unfavorable to the solution-processed HTL. Furthermore, it has been reported that some dopants like Li-TFSI could cause different degrees of hysteresis.[32] Hence, it is an urgent demand to discover an efficient and organic-soluble dopant for the rapid oxidation of HTLs.

As we known, benzoquinone-based 2,3-dichloro-5,6-dicyano-1,4-benzoquinone (DDQ) is a strong electron π-acceptor, which has been generally used as a catalyst in chemical synthesis and exhibits good solubility in organic solvents.[33,34] Moreover, it can

Engineering Research Center of Environment-Friendly Functional Materials, Ministry of Education, Fujian Engineering Research Center of Green Functional Materials, Institute of Materials Physical Chemistry, Huaqiao University, Xiamen, 361021, China. E-mail: sunweihai@hqu.edu.cn; jhwu@hqu.edu.cn

† Electronic supplementary information (ESI) available. See DOI: 10.1039/d0ra07254k

easily form a charge transfer DDQ–donor complex by reacting with an electron donor.[35,36] Recently, Sun *et al.* demonstrated that DDQ could be a promising p-dopant for triphenylamine-based oligomer HTM named MeO-TPD in solid-state dye-sensitized solar cells.[37] Therefore, we employed DDQ as a p-type dopant into spiro-OMeTAD HTL for highly efficient PSCs. The optical test results reveal that spiro-OMeTAD could be quickly oxidized by DDQ and the more spiro-OMeTAD$^{+\bullet}$ cation radicals are generated, thereby increasing the conductivity of HTL and adjusting the energy level of spiro-OMeTAD, and it is also verified by the Tafel, PL, TRPL and UPS measurements. The influences of the dopant concentration on the device performances were systematically studied. Eventually, the champion PSC based on spiro-OMeTAD HTL incorporated with DDQ delivers a remarkable efficiency of 21.16%, which is improved by 16% than that of the control PSC. Furthermore, the planar PSCs employing DDQ-doped HTL demonstrate superior stability and mitigated hysteresis, which renders that DDQ is an excellent p-type dopant of HTL for highly efficient and long-term stable PSCs.

2. Experimental section

2.1. Materials

The fluorine-doped tin oxide (FTO) coated glass substrate was obtained from Liaoning You Xuan Tech Co., Ltd. Unless specifically stated, all chemicals are used directly without further purification, including CsI, $PbBr_2$ and PbI_2 (99.99%, TCI), 2,3-dichloro-5,6-dicyano-1,4-benzoquinone (98%, Innochem), spiro-OMeTAD (>98%, Luminescence Technology Corp, Taiwan, China), Li-TFSI and *t*BP (99%, Sigma-Aldrich), FAI and MABr (99.50%, Xi'an Polymer Light Technology Co., Ltd).

2.2. Device fabrication

The FTO glass was washed by sonication in detergent, water, acetone, and isopropanol consecutively for 20 min and then dried by N_2. Before using, the FTO substrate was further treated by UV–ozone cleaning for 25 min and plasma for another 5 min.

The colloidal TiO_2 quantum dots were prepared *via* a simple solvothermal method according to the previous literature.[38] The compact TiO_2 layer was deposited by spin-coating the colloidal solution onto the FTO glass at 4000 rpm for 60 s and then annealed at 500 °C for 0.5 h. Afterwards, the substrates were moved to the N_2-filled glove box.

The perovskite precursor solution was prepared as previously reported. $PbBr_2$ (0.20 M), MABr (0.20 M), PbI_2 (1.15 M), CsI (0.07 M) and FAI (1.00 M) were dissolved in a mixed solution of dimethyl sulfoxide (DMSO) and *N*,*N*-dimethylformamide (DMF), of which the volume ratio is 1 : 4. The solution was stirring for at least 6 h and filtrated with 0.45 μm PTFE filters. The precursor solution was deposited through a two-steps program at 1000 rpm and 6500 rpm for 10 s and 30 s, respectively. 120 μL of chlorobenzene (CB) as an anti-solvent was quickly dripped onto the spinning substrates after 15 s in the second process. Then, the as-prepared layers were annealed at 100 °C for 1 h.

For the preparation of spiro-OMeTAD solution, 17.5 μL Li-TFSI solution (0.55 mM, acetonitrile), 28.6 μL *t*BP and 75.0 mg spiro-OMeTAD were mixed in 1 mL CB and stirred for 3 h. For comparison, the DDQ doped spiro-OMeTAD solution, DDQ with different molar ratio was added into the prepared spiro-OMeTAD solution containing both *t*BP and Li-TFSI. The HTLs were formed *via* spin-coating aforementioned solution at 5000 rpm for 30 s. For simplicity, we refer to the pristine spiro-OMeTAD with none additives as P-spiro-OMeTAD, the spiro-OMeTAD with *t*BP and Li-TFSI as U-spiro-OMeTAD, and the spiro-OMeTAD with DDQ as D-spiro-OMeTAD. The as-formed U-spiro-OMeTAD films were moved to a dry cabinet (humidity < 15%) in the dark overnight to complete oxidation for HTL. For comparison, the D-spiro-OMeTAD HTLs were immediately used in the next step.

Finally, a gold electrode with 80 nm thickness was fabricated by thermal evaporation.

2.3. Characterization

The ultraviolet-visible absorption spectra of virous HTM solutions were obtained through a UV-visible-NIR spectrophotometer (Shimadzu UV-2550, Japan). A Hitachi S-8000 field-emission scanning electron microscope was used to measure the SEM images. The UPS measurements were recorded on a Thermo Fisher Scientific ESCALAB 250 Xi instrument. Steady-state photoluminescence (PL) spectra were acquired using a Thermo Scientific Lumina LF-1303003 fluorescence spectrophotometer. Time-resolved photoluminescence (TRPL) spectra were measured by a spectrograph (Zolix) with an Omin-λ monochromator. The photocurrent density–voltage (*J*–*V*) curves of PSCs device were recorded in an ambient air under simulated 100 mW cm^{-2} (AM 1.5 G) with a 3A solar simulator (PVIV-94043A, Newport, USA) by a computer-controlled Keithley 2420 source meter, which was calibrated by a silicon solar cell (NREL, USA) with a KG-2 filter. The electrochemical impedance spectroscopy (EIS) of devices were tested by an electrochemical workstation (Zahner IM6e, Germany) in the dark.

3. Results and discussion

As we known, the oxidation potential of DDQ/[DDQ]$^{-\bullet}$ (0.755 V, NHE)[39] is a little higher than that of [spiro-OMeTAD]$^{+\bullet}$/spiro-OMeTAD (0.63 V, NHE).[40] Thus, it can offer a sufficient driving power for the generation of oxidized spiro-OMeTAD. To illustrate the oxidation ability of DDQ, we grinded DDQ into spiro-OMeTAD as solid state in a mortar. The color of spiro-OMeTAD directly changed from white to deep brown when DDQ was added (Fig. 1a), indicating spiro-OMeTAD is oxidized by DDQ. A similar phenomenon has also occurred in the form of spiro-OMeTAD solution (Fig. 1b). After the addition of DDQ into the spiro-OMeTAD solution, we observed apparent color variation from light yellow to pale brown, which is normally associated with oxidized spiro-OMeTAD.

Fig. 1c displays the UV-vis absorption spectra of P-spiro-OMeTAD, U-spiro-OMeTAD and D-spiro-OMeTAD. As can be seen, all of the solution exhibit strong absorption band of spiro-

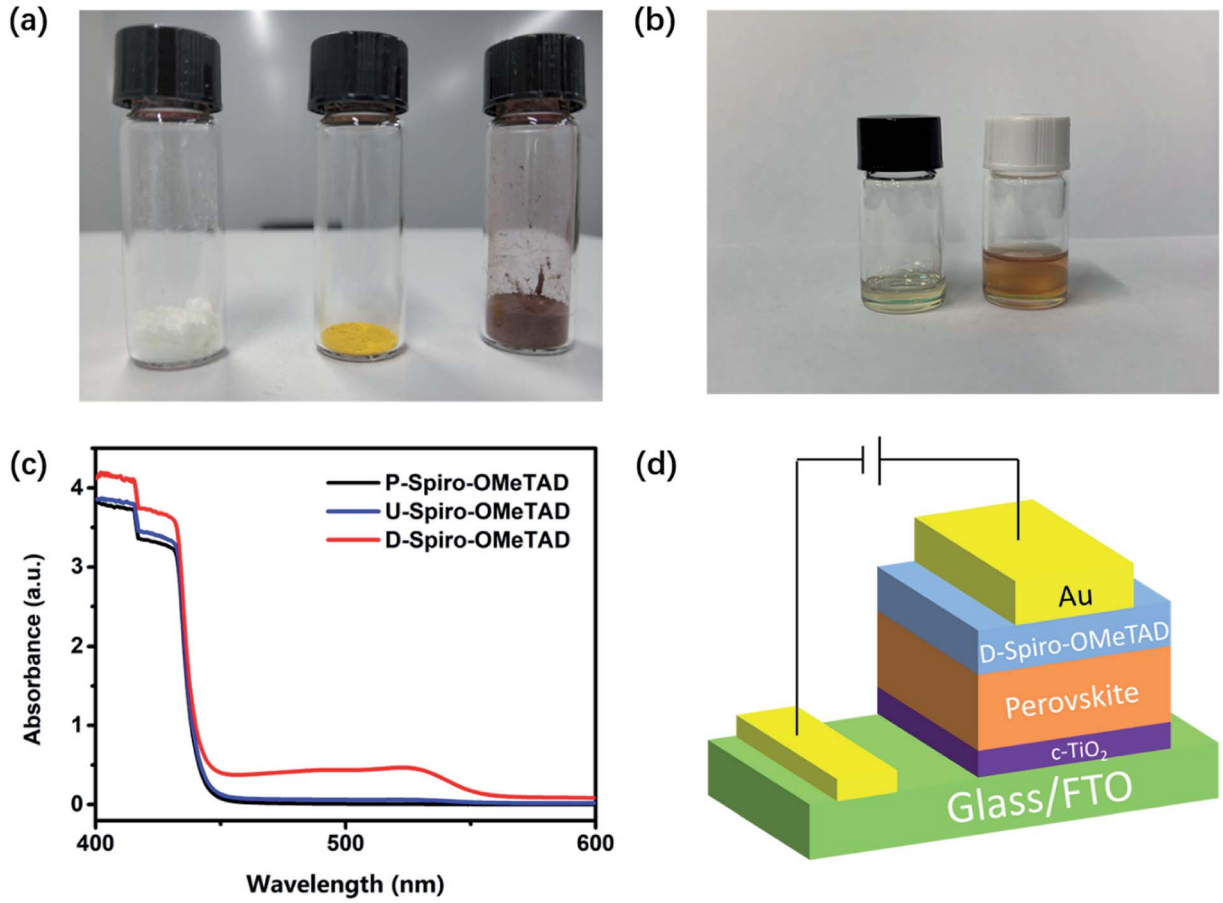

Fig. 1 (a) Photos of DDQ (middle), pure spiro-OMeTAD (left) and a mixture of them (right) in solid state. (b) Photos of D-spiro-OMeTAD (right) and U-spiro-OMeTAD (left) in chlorobenzene solution. (c) UV-vis absorption spectra of P-spiro-OMeTAD, U-spiro-OMeTAD and D-spiro-OMeTAD. (d) Schematic illustration of the architecture of PSC.

OMeTAD at about 390 nm. It is obvious that a new intense absorption peak at around 500 nm arises in the D-spiro-OMeTAD solution, compared with that of P-spiro-OMeTAD and U-spiro-OMeTAD, suggesting charge transfer takes place between DDQ and spiro-OMeTAD.[37] In order to confirm the formation of charge–transfer complex in DDQ doped spiro-OMeTAD, Fourier-transform infrared (FTIR) spectra were performed. As shown in Fig. S1,† the stretching band of the nitrile (CN) group in the pure DDQ appears at 2233 cm^{-1}, while it shifts to 2208 cm^{-1} after blending with spiro-OMeTAD, indicating that the electron transfer from spiro-OMeTAD to DDQ occurs and thus the formation of charge–transfer complex could be expected.[37] As the charge–transfer complex is generated, it would leave holes in spiro-OMeTAD and increase the electrical conductivity as well as hole mobility of final HTL in devices for better photovoltaic performance.[41] Therefore, the doping mechanism may be described as follows:

$$\text{Spiro-OMeTAD} + \text{DDQ} \overset{\text{fast}}{\rightarrow} [\text{spiro-OMeTAD}]^{+\cdot}[\text{DDQ}]^{-\cdot}$$

The device comprising a configuration of FTO/compact TiO_2/perovskite/HTL/Au was prepared (Fig. 1d), and Fig. 2a displays the related cross-sectional SEM image of device. The current–voltage (J–V) characteristics of devices with HTLs incorporated with different concentration of DDQ and their corresponding photovoltaic parameters are shown in Fig. 2b and Table 1. Expectedly, all of the devices with the incorporation of DDQ exhibits an increased PCE compared to that of PSC with the HTL without DDQ. The champion device with the 0.06% DDQ dopant delivers an impressive PCE of 21.16%, with a short-circuit current density (J_{SC}) of 22.92 mA cm^{-2}, a V_{OC} of 1.16 V and an FF of 0.796, whereas the undoped PSC shows a relatively lower PCE of 18.24%, with a J_{SC} of 22.54 mA cm^{-2}, a V_{OC} of 1.10 V and an FF of 0.736. The increase of PCE is ascribed to the significantly enhanced both of FF and V_{OC}, indicative of the improved conductivity, adequate energy level and increased charge extraction capability of doped HTL, which will be discussed below.

To gain insights into the increased FF and V_{OC} of the devices with the DDQ doped HTL, the shunt resistance (R_{sh}) and series resistance (R_s) could be extrapolated directly from the illuminated J–V characteristics of PSCs (Fig. 2b) and displayed in Table 1. As can be seen, the undoped sample shows a higher R_s and lower R_{sh}, whereas in the DDQ sample, lower R_s and higher R_{sh}. It is well known that a lower R_s and higher R_{sh} of device can result in a higher FF and V_{OC}, owing to the high hole mobility

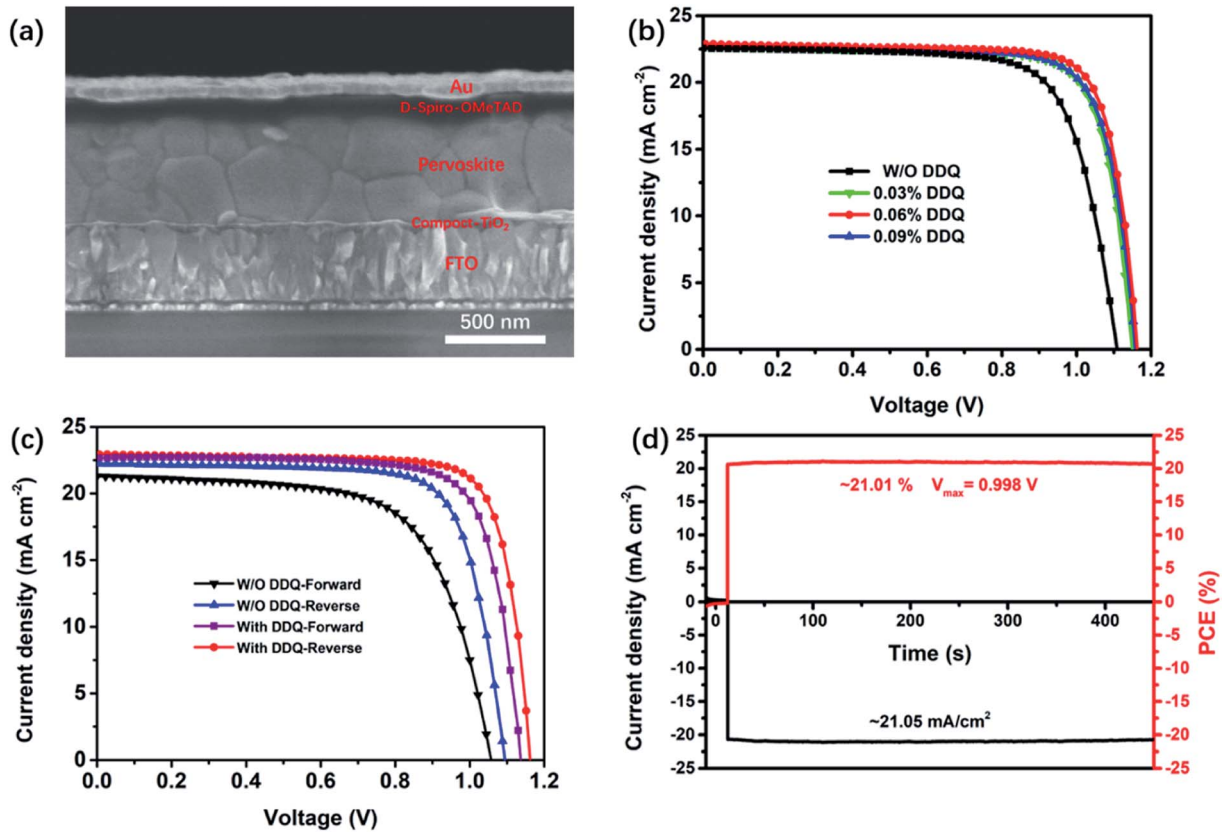

Fig. 2 (a) SEM of cross-sectional image of the corresponding device with D-spiro-OMeTAD film. (b) *J–V* characteristics of devices with HTLs doped by various concentration of DDQ. (c) *J–V* characteristics of PSCs using spiro-OMeTAD with and W/O DDQ, measured at both forward and reverse scanning directions. (d) The steady-state J_{SC} and PCE output of the optimal PSC using DDQ doped HTL.

and conductivity of doped HTL, and the suppressed non-radiative combination at interfaces between the HTL and perovskite layer.

Along with the improvement in V_{OC} and FF, the DDQ doping leads to a suppressed hysteresis, as well as the higher steady-state efficiencies. During the measurements of PSCs, the hysteresis is a general issue that the shapes of *J–V* characteristics are changed with the different scanning directions and rates.[42] The more serious hysteresis has been found in the PSCs with a planar n–i–p architecture comprising compact TiO_2 ETL.[43] The mechanism of hysteresis in PSCs is unclear and still under debate, associated with various factors such as the ferroelectric effect, ion migration, unbalanced charge transportation and charge recombination.[44,45] To gauge the degree of hysteresis, the hysteresis index (HI) is often obtained by the following mathematical formula: $HI = (PCE_{reverse} - PCE_{forward})/PCE_{reverse}$. Fig. 2c shows the *J–V* characteristics of the device based on DDQ doped HTL and the reference device using different scans, and the corresponding photovoltaic data are given in Table 2. Notably, the HI for DDQ modified PSC is only 0.055, smaller than that for undoped device. Although hysteresis still exists in our devices, such small hysteresis is relatively rare in planar TiO_2-based PSCs.[46] Moreover, the steady state photocurrent and PCE output recorded at a bias voltage of 0.99 V maintained a stable J_{SC} of 21.05 mA cm^{-2} and a steady-state PCE of 20.84% (Fig. 2d), approximated to the PCE achieved by the *J–V* characteristics, confirming the minor hysteresis and the reliability of *J–V* measurement in the DDQ-based devices. The mitigated hysteresis is mainly attributed to the improved electrical properties of HTL and the passivation for the defects at the interface and boundaries of perovskite layer by DDQ.

Table 1 Photovoltaic data of the devices with various concentration of DDQ doped spiro-OMeTAD

DDQ concentration	V_{OC} (V)	J_{SC} (mA cm^{-2})	FF	PCE (%)	R_{sh} (kΩ cm^2)	R_s (Ω cm^2)
0	1.10	22.54	0.736	18.24	3.01	5.48
0.03%	1.15	22.66	0.779	20.30	3.65	2.91
0.06%	1.16	22.92	0.796	21.16	4.01	2.87
0.09%	1.15	22.67	0.780	20.33	3.38	3.55

Table 2 Photovoltaic data of DDQ modified device and the reference device with forward and reverse scanning directions

Device	Scanning directions	V_{OC} (V)	J_{SC} (mA cm^{-2})	FF	PCE (%)	HI
Reference	Forward	1.07	21.73	0.669	15.55	0.147
	Reverse	1.09	22.23	0.753	18.24	
DDQ modified	Forward	1.14	22.69	0.771	19.94	0.055
	Reverse	1.16	22.86	0.795	21.08	

To probe the reproducibility of the device efficiency, 30 independent devices without and with DDQ were fabricated and measured. Fig. 3 shows the statistical data of devices. The distribution of PCEs for the devices with DDQ is basically focused on a small range from 20% to 21%, higher than that of devices without DDQ (from 17% to 18%), which is in line with the values obtained from the stabilized power output measurements. Based on the statistical results, the narrower range of the data achieved by the DDQ doped devices indicate the excellent reproducibility of our PSCs fabrication procedure. Therefore, the above results provide a possible opportunity for reducing hysteresis issue and improving the repeatability of PSCs by the doping HTLs.

To better understand the effect of the dopants on the energy level of HTLs, ultraviolet photoemission spectra (UPS) were performed and displayed in Fig. 4a and b. The conduction band maximum (E_{CB}), valence band maximum (E_{VB}), and the Fermi level (E_F) could be obtained according to the equations: $E_{CB} = E_{VB} + E_g$ (energy bandgap), $E_{VB} = E_F - E_{onset}$ (onset energy), and $E_F = E_{cut\text{-}off}$ (cut-off energy) $- 21.22$ eV.[47,48] The UV-visible Tauc plots of HTLs (Fig. 4c) were extracted to analyze the E_g, by the equation: $A(h\nu - E_g) = (\alpha h\nu)^2$, where A is the proportional constant and α is the absorption constant. The detailed values of energy level for the different spiro-OMeTAD HTLs are summarized in Table 3. After the DDQ doping, the calculated Fermi level value of spiro-OMeTAD films shifted downward from -4.67 eV to -4.78 eV, indicative of the formation of extensive p-type oxidized spiro-OMeTAD cation and responsible for the increased conductivity. The energy levels diagram of perovskite and various spiro-OMeTAD films is illustrated in Fig. 4d. Obviously, the E_{VB} of spiro-OMeTAD films reduced from -4.99 eV to -5.10 eV after the addition of DDQ. A downshift of the E_{VB} for spiro-OMeTAD doped with DDQ is closer to the E_{VB} of perovskite, demonstrating a better energy level match between perovskite layer and HTLs and efficient hole extraction between perovskite and the doped HTL, which accounts for the enhancement of the V_{OC} in the DDQ-based devices.

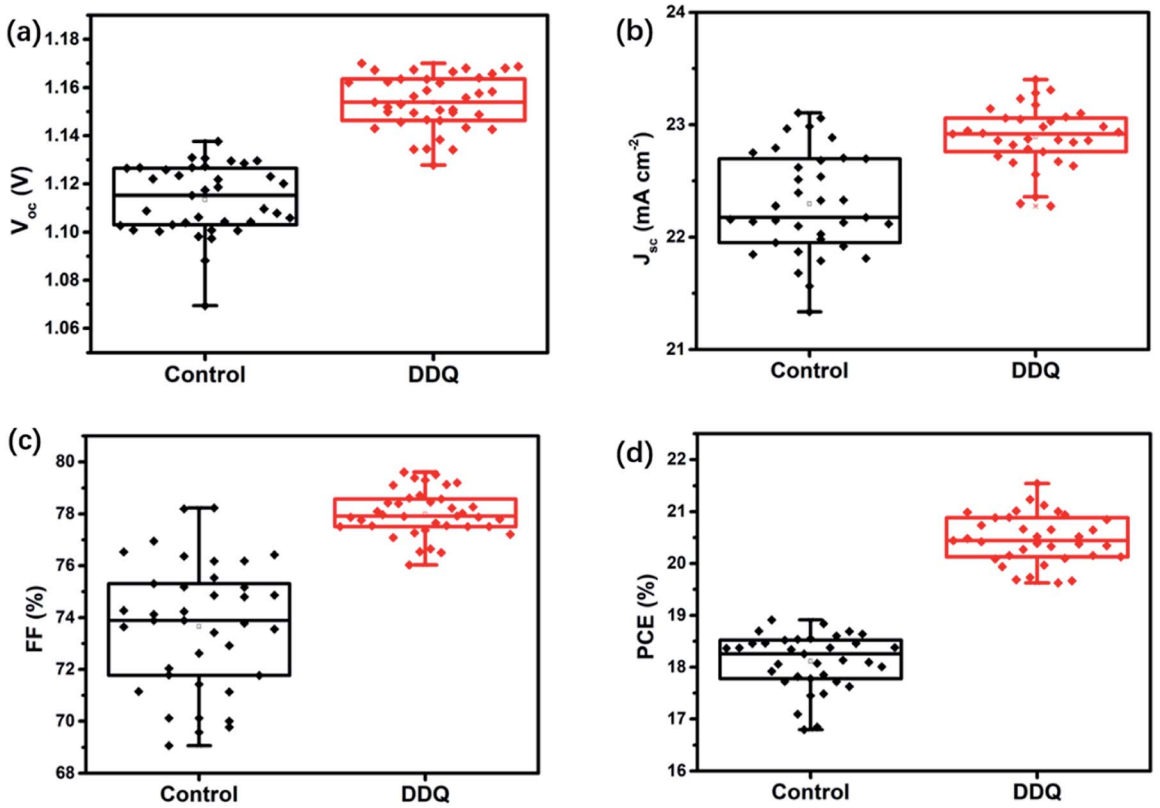

Fig. 3 The statistical data based on 30 independent control and DDQ doped devices: (a) V_{OC}, (b) J_{SC}, (c) FF and (d) PCE.

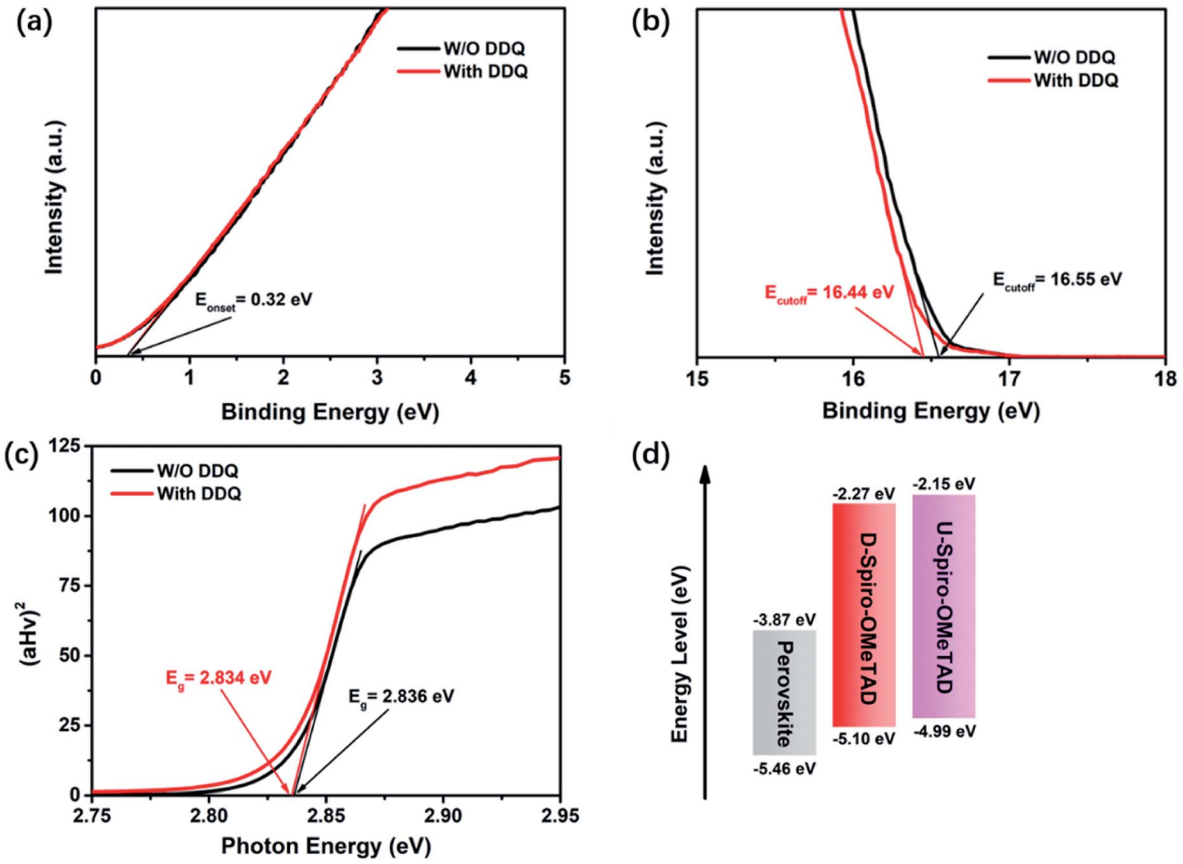

Fig. 4 UPS of the spiro-OMeTAD films with or W/O DDQ incorporation: (a) E_{onset} region, (b) E_{cutoff} region. (c) Tauc plots of the HTLs with or W/O DDQ. (d) Energy levels of the perovskite and various HTLs.

The hole extraction between perovskite and HTLs was examined by the steady-state photoluminescence (PL) and time-resolved photoluminescence (TRPL) spectroscopy. As can be seen from Fig. 5a, the perovskite film exhibits a distinct PL emission peak at 760 nm derived from the exciton recombination in perovskite layer. Intense PL quenching is noticed when covered by U-spiro-OMeTAD HTL, offering hole extraction from perovskite to HTL. Furthermore, a continuous and substantial PL quenching was noticed with the addition of DDQ into spiro-OMeTAD, implying that D-spiro-OMeTAD HTL could extract holes from perovskite more efficiently. And this point is also corroborated by the TRPL decay (Fig. 5b) and the relevant parameters determined by a bi-exponential decay function are given in Table 4. The bi-exponential PL decay process is comprised of two decay components, of which the short lifetime (τ_1) is originated from the nonradiative losses by the quenching of charge carriers using carrier transport layer and the long lifetime (τ_2) is stemmed from the radiative recombination, respectively.[49] The perovskite layer exhibits a PL decay lifetime ($\tau_1 = 10.71$ ns, $\tau_2 = 124.67$ ns). After being covered with spiro-OMeTAD, the PL decay lifetime for the sample of FTO/perovskite/D-spiro-OMeTAD ($\tau_1 = 6.70$ ns, $\tau_2 = 23.89$ ns) was shorter than those of the sample of FTO/perovskite/U-spiro-OMeTAD ($\tau_1 = 11.18$ ns, $\tau_2 = 57.97$ ns), indicative of the effective hole transfer between perovskite and D-spiro-OMeTAD layers, which is indispensable for superior charge extraction and collection in PSCs.

To estimate the effect of DDQ dopant on the electrical properties in the HTLs, the Tafel curves of devices based on spiro-OMeTAD HTLs with and without DDQ were measured and presented in Fig. 5c. Notably, the spiro-OMeTAD HTL with DDQ based device exhibits higher current density than that of the undoped one, implying that the conductivity of HTL is enhanced after doping DDQ. The increased conductivity of HTL is due to the more free generated holes after incorporation of DDQ into spiro-OMeTAD film.

Table 3 The calculated values of energy level of the HTLs doped with and without DDQ

HTL	E_{onset} (eV)	E_{cutoff} (eV)	E_F (eV)	E_g (eV)	E_{VB} (eV)	E_{CB} (eV)
Without DDQ	0.32	16.55	−4.67	2.83	−4.99	−2.16
With DDQ	0.32	16.44	−4.78	2.83	−5.10	−2.27

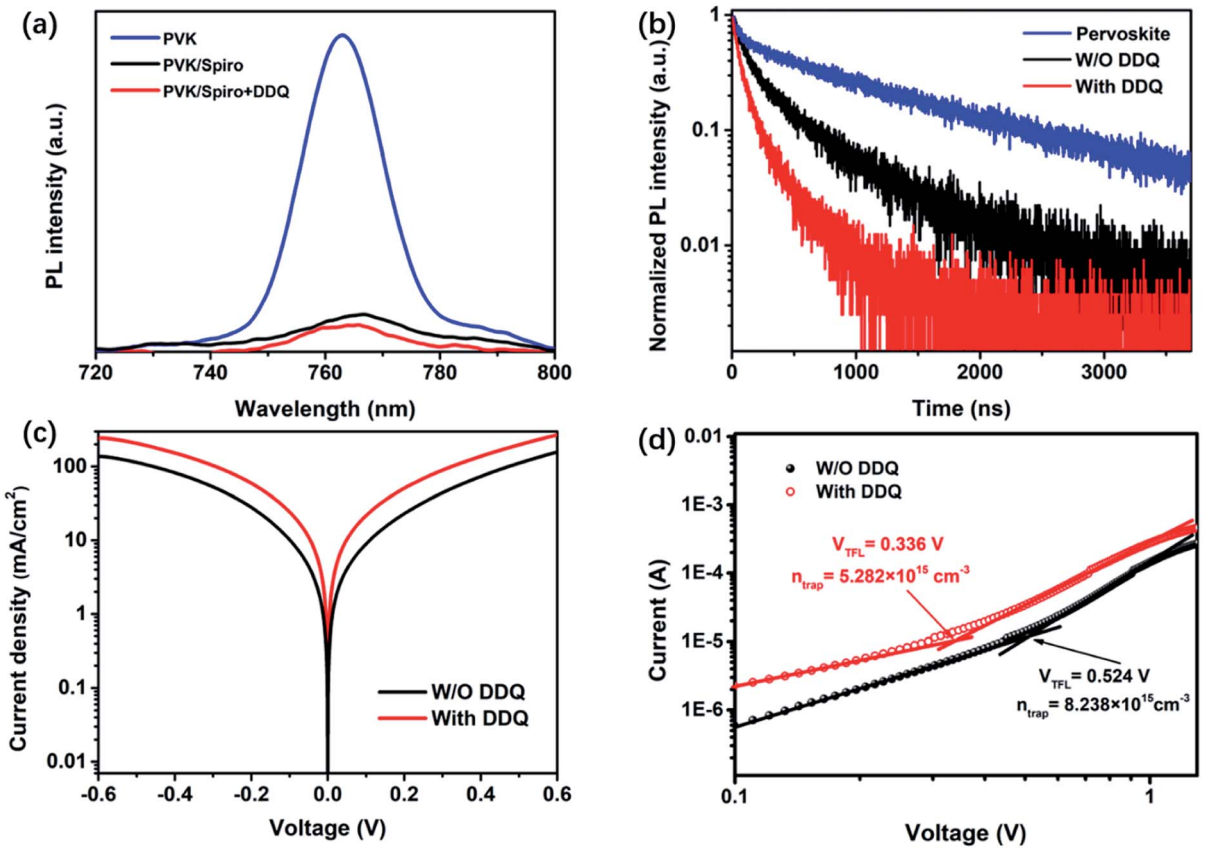

Fig. 5 (a) PL spectra and (b) TRPL spectra of pristine perovskite and perovskite/spiro-OMeTAD with different dopants. (c) Tafel plots of devices based on HTLs with and W/O DDQ. (d) Dark J–V curves of hole-only devices based on spiro-OMeTAD HTL with and W/O DDQ.

Table 4 TRPL data of FTO/perovskite and FTO/perovskite/spiro-OMeTAD with various dopants

Samples	A_1 (%)	τ_1 (ns)	A_2 (%)	τ_2 (ns)
FTO/perovskite	27.77	10.71	72.23	124.67
FTO/perovskite/U-spiro-OMeTAD	63.52	11.18	36.48	57.97
FTO/perovskite/D-spiro-OMeTAD	75.86	6.70	24.14	23.89

The hole-only devices based on a configuration of FTO/PEDOT:PSS/perovskite/HTL (with or without DDQ)/Au were performed under dark condition to estimate the trap density (n_{trap}) in the PSC according to the equation of $n_{trap} = 2\varepsilon\varepsilon_0 V_{TFL}/eL^2$,[50,51] where ε_0 is the vacuum permittivity, ε is a relative dielectric constant of perovskite,[52] V_{TFL} is the trap-filled limit voltage, L represents the thickness of the perovskite layer, and e is an elementary charge of the electron as shown in Fig. 5d. The n_{trap} of the device with DDQ is 5.28×10^{15} cm^{-3}, lower than that of device without DDQ (8.24×10^{15} cm^{-3}), due to the effective suppression of trap state within perovskite layer by the DDQ doped HTL. There are many reports about the trap states or defects in perovskite films passivated substantially by the additives of organic molecules with functional groups such as carboxyl, amino, halogen and cyano, either in perovskite films or as interfacial layer.[53,54] In our case, DDQ as a strong electron acceptor could react with halide ions in perovskite to form anion–π complexes,[39] thus passivating traps and alleviating hysteresis, similar to the function of another organic dopant F4-TCNQ for spiro-OMeTAD in the earlier work.[55]

Further insight of the charge recombination mechanisms and the enlargement of V_{OC} in the devices with DDQ doped HTL was attained by recording V_{OC} at different light intensities. Fig. 6a shows the V_{OC} *versus* light intensity. It has been reported that light intensity-dependent V_{OC} is correlated with the charge recombination process in photovoltaic device; in other words, the fitted slope is equal to 1, indicative of bimolecular recombination, while trap-assisted recombination mainly exists when the slope equals 2.[56] As for the device with DDQ-incorporated HTL, its V_{OC} value exhibits a fitted slope of 1.151 kT/q; while the slope increases to 1.330 for the device without DDQ incorporation. The smaller slope of DDQ-based device suggests the suppressed trap-assisted recombination in the PSC using DDQ, which is consistence with the reduced trap density as mentioned above.

We further employed the electrical impedance spectra (EIS) to test the charge transfer properties in PSCs with or without DDQ doped HTLs in the dark. It is noted that the Nyquist plots usually have two semicircles, where the semicircle at low frequency is typically considered as the charge recombination process in the devices.[57] As shown in Fig. 6b, there is only one

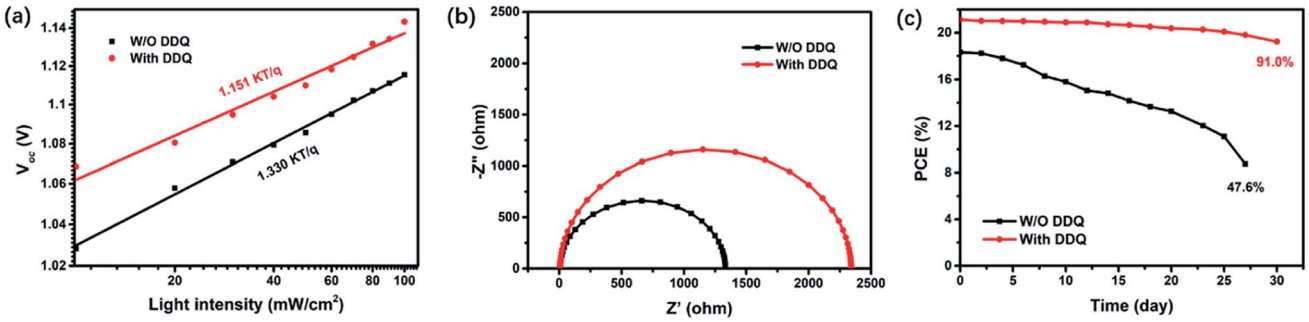

Fig. 6 (a) V_{OC} values of the PSCs using the HTLs with or W/O DDQ as a function of light intensity. (b) Nyquist plots of the PSCs doped with or W/O DDQ obtained in the dark condition. (c) Stability test for the efficiencies of the unpackaged devices based on doped or undoped spiro-OMeTAD HTLs.

semicircle observed in the low frequency region, which is probably ascribed to two reasons: one is the enhancement in the recombination resistance in the dark conditions[58,59] and the other is that the interface between perovskite and spiro-OMeTAD is an ohmic contact rather than rectifying contact.[60,61] The radius of semicircle for the DDQ modified device is significantly bigger with respect to that of semicircle for unmodified device, suggesting that continuously reduced nonradiative recombination rate and consequently the higher V_{OC}. This result is also consistent with that of PL measurements aforementioned.

The stability of the PSCs with or without DDQ doping for spiro-OMeTAD were conducted without any encapsulation for about 30 days (humidity: ~20%, temperature: 25 °C, dark condition, Fig. 6c). The PCE of reference cell dramatically attenuated to half of the original value after 27 days storage, while the device with DDQ maintained 91% of its initial PCE, demonstrating a superior long-term stability of DDQ doped PSCs. Additionally, the evolutions of the other device parameters (V_{OC}, J_{SC} and FF) for devices are also displayed in Fig. S2.† For the case of reference devices, the degradation rate of FF exhibited much more pronounced in contrast to the V_{OC} and J_{SC}, while DDQ treatment enabled FF relatively more stable. There are two possible reasons for the excellent device stability, one is the reduction of trap density in the interface and grain boundaries of the perovskite film, and another one is the shortened of the oxidation time for spiro-OMeTAD in humid air exposure. Thus, the impressive device stability enables DDQ as a potential additive of HTM for practical device applications.

4. Conclusion

We developed a facile and effective method for introducing DDQ as an excellent dopant into spiro-OMeTAD and investigated its application in PSCs. The results of optical spectra indicated spiro-OMeTAD could be rapidly changed into spiro-OMeTAD$^{+\bullet}$ cation radicals by the dopant DDQ. The UPS, Tafel, PL, TRPL, and EIS analysis offered an evidence that the down-shift of the Fermi level, the enhanced conductivity, fast hole extraction and transport ability of doped HTL lead to the improved V_{OC}, FF and PCE, simultaneously. Eventually, the planar PSCs employing DDQ doped spiro-OMeTAD as HTL achieved an optimal PCE of 21.16%, which is increased by 16% compared with that of devices without DDQ doping. More importantly, the devices based on DDQ demonstrated significantly suppressed hysteresis, excellent stability, shorter preparation time and good reproducibility. This study provides an important guidance for the future growth of efficient dopants of spiro-OMeTAD for highly efficient and long-term stability PSCs.

Conflicts of interest

There are no conflicts to declare.

Acknowledgements

We are thankful to the National Natural Science Foundation of China (No. U1705256, 21771066, 51972123 and 61804058) and the Promotion Program for Young and Middle-aged Teacher in Science and Technology Research of Huaqiao University (ZQN-706).

References

1 E. H. Jung, N. J. Jeon, E. Y. Park, C. S. Moon, T. J. Shin, T.-Y. Yang, J. H. Noh and J. Seo, *Nature*, 2019, **567**, 511–515.
2 H. J. Snaith, *J. Phys. Chem. Lett.*, 2013, **4**, 3623–3630.
3 P. Docampo, J. M. Ball, M. Darwich, G. E. Eperon and H. J. Snaith, *Nat. Commun.*, 2013, **4**, 3761.
4 J. M. Ball, M. M. Lee, A. Hey and H. J. Snaith, *Energy Environ. Sci.*, 2013, **6**, 1739–1743.
5 Z. Song, C. L. McElvany, A. B. Phillips, I. Celik, P. W. Krantz, S. C. Watthage, G. K. Liyanage, D. Apul and M. J. Heben, *Energy Environ. Sci.*, 2017, **10**, 1297–1305.
6 D. P. McMeekin, S. Mahesh, N. K. Noel, M. T. Klug, J. Lim, J. H. Warby, J. M. Ball, L. M. Herz, M. B. Johnston and H. J. Snaith, *Joule*, 2019, **3**, 387–401.
7 M. M. Lee, J. Teuscher, T. Miyasaka, T. N. Murakami and H. J. Snaith, *Science*, 2012, **338**, 643–647.
8 H. S. Kim, C. R. Lee, J. H. Im, K. B. Lee, T. Moehl, A. Marchioro, S. J. Moon, R. Humphry-Baker, J. H. Yum, J. E. Moser, M. Gratzel and N. G. Park, *Sci. Rep.*, 2012, **2**, 591.

9 *Best Research Cell Efficiencies*, https://www.nrel.gov/pv/assets/pdfs/best-research-cell-efficiencies.20200218.pdf, accessed, February 2020.
10 G.-W. Kim, H. Choi, M. Kim, J. Lee, S. Y. Son and T. Park, *Adv. Energy Mater.*, 2020, **10**, 1903403.
11 J. Urieta-Mora, I. García-Benito, A. Molina-Ontoria and N. Martín, *Chem. Soc. Rev.*, 2018, **47**, 8541–8571.
12 W. Sun, Y. Li, S. Ye, H. Rao, W. Yan, H. Peng, Y. Li, Z. Liu, S. Wang, Z. Chen, L. Xiao, Z. Bian and C. Huang, *Nanoscale*, 2016, **8**, 10806–10813.
13 W. Sun, S. Ye, H. Rao, Y. Li, Z. Liu, L. Xiao, Z. Chen, Z. Bian and C. Huang, *Nanoscale*, 2016, **8**, 15954–15960.
14 W. Sun, Y. Li, Y. Xiao, Z. Zhao, S. Ye, H. Rao, H. Ting, Z. Bian, L. Xiao, C. Huang and Z. Chen, *Org. Electron.*, 2017, **46**, 22–27.
15 J. Burschka, A. Dualeh, F. Kessler, E. Baranoff, N.-L. Cevey-Ha, C. Yi, M. K. Nazeeruddin and M. Grätzel, *J. Am. Chem. Soc.*, 2011, **133**, 18042–18045.
16 H. J. Snaith, A. J. Moule, C. Klein, K. Meerholz, R. H. Friend and M. Grätzel, *Nano Lett.*, 2007, **7**, 3372–3376.
17 J. Dewalque, P. Colson, G. K. V. V. Thalluri, F. Mathis, G. Chêne, R. Cloots and C. Henrist, *Org. Electron.*, 2014, **15**, 9–15.
18 F. Fabregat-Santiago, J. Bisquert, L. Cevey, P. Chen, M. Wang, S. M. Zakeeruddin and M. Grätzel, *J. Am. Chem. Soc.*, 2009, **131**, 558–562.
19 T. Leijtens, I. K. Ding, T. Giovenzana, J. T. Bloking, M. D. McGehee and A. Sellinger, *ACS Nano*, 2012, **6**, 1455–1462.
20 T. H. Schloemer, J. A. Christians, J. M. Luther and A. Sellinger, *Chem. Sci.*, 2019, **10**, 1904–1935.
21 H. J. Snaith and M. Grätzel, *Appl. Phys. Lett.*, 2006, **89**, 262114.
22 J. H. Noh, N. J. Jeon, Y. C. Choi, M. K. Nazeeruddin, M. Grätzel and S. I. Seok, *J. Mater. Chem. A*, 2013, **1**, 11842–11847.
23 S. Ghosh and T. Singh, *Nano Energy*, 2019, **63**, 103828.
24 D.-Y. Chen, W.-H. Tseng, S.-P. Liang, C.-I. Wu, C.-W. Hsu, Y. Chi, W.-Y. Hung and P.-T. Chou, *Phys. Chem. Chem. Phys.*, 2012, **14**, 11689–11694.
25 E. J. Juarez-Perez, M. R. Leyden, S. Wang, L. K. Ono, Z. Hawash and Y. Qi, *Chem. Mater.*, 2016, **28**, 5702–5709.
26 L. K. Ono, P. Schulz, J. J. Endres, G. O. Nikiforov, Y. Kato, A. Kahn and Y. Qi, *J. Phys. Chem. Lett.*, 2014, **5**, 1374–1379.
27 A. Abate, T. Leijtens, S. Pathak, J. Teuscher, R. Avolio, M. E. Errico, J. Kirkpatrik, J. M. Ball, P. Docampo, I. McPherson and H. J. Snaith, *Phys. Chem. Chem. Phys.*, 2013, **15**, 2572–2579.
28 X. Gu, Y. Li, Y. Mu, M. Zhang, T. Lu and P. Wang, *RSC Adv.*, 2018, **8**, 9409–9413.
29 M. Xu, Y. Rong, Z. Ku, A. Mei, X. Li and H. Han, *J. Phys. Chem. C*, 2013, **117**, 22492–22496.
30 Y. Yang, J. Wu, X. Liu, Q. Guo, X. Wang, L. Liu, Y. Ding, S. Dai and J.-Y. Lin, *ACS Appl. Energy Mater.*, 2019, **2**, 2188–2196.
31 X. Wang, J. Wu, Y. Yang, X. Liu, Q. Guo, Z. Song, G. Li, Z. Lan and M. Huang, *J. Mater. Chem. A*, 2019, **7**, 13256–13264.
32 J. Luo, J. Xia, H. Yang, L. Chen, Z. Wan, F. Han, H. A. Malik, X. Zhu and C. Jia, *Energy Environ. Sci.*, 2018, **11**, 2035–2045.
33 K. Ohkubo, A. Fujimoto and S. Fukuzumi, *J. Am. Chem. Soc.*, 2013, **135**, 5368–5371.
34 L. Liu and P. E. Floreancig, *Org. Lett.*, 2010, **12**, 4686–4689.
35 M. Hasani, M. Shariati-Rad and H. Abdollahi, *Anal. Chim. Acta*, 2009, **636**, 175–182.
36 V. Abbu, V. Nampally, N. Baindla and P. Tigulla, *J. Solution Chem.*, 2019, **48**, 61–81.
37 Y. Zhang, X. Yang, W. Wang, X. Wang and L. Sun, *J. Energy Chem.*, 2018, **27**, 413–418.
38 Y. Tu, J. Wu, M. Zheng, J. Huo, P. Zhou, Z. Lan, J. Lin and M. Huang, *Nanoscale*, 2015, **7**, 20539–20546.
39 S. Kepler, M. Zeller and S. V. Rosokha, *J. Am. Chem. Soc.*, 2019, **141**, 9338–9348.
40 B. Xu, H. Tian, D. Bi, E. Gabrielsson, E. M. J. Johansson, G. Boschloo, A. Hagfeldt and L. Sun, *J. Mater. Chem. A*, 2013, **1**, 14467–14470.
41 W. Wang, X. Yang, J. Li, H. Wang, J. An, L. Zhang, X. Jiang, Z. Yu and L. Sun, *Energy Technol.*, 2018, **6**, 752–758.
42 H. J. Snaith, A. Abate, J. M. Ball, G. E. Eperon, T. Leijtens, N. K. Noel, S. D. Stranks, J. T.-W. Wang, K. Wojciechowski and W. Zhang, *J. Phys. Chem. Lett.*, 2014, **5**, 1511–1515.
43 Y. Zhang, M. Liu, G. E. Eperon, T. C. Leijtens, D. McMeekin, M. Saliba, W. Zhang, M. de Bastiani, A. Petrozza, L. M. Herz, M. B. Johnston, H. Lin and H. J. Snaith, *Mater. Horiz.*, 2015, **2**, 315–322.
44 B. Chen, M. Yang, S. Priya and K. Zhu, *J. Phys. Chem. Lett.*, 2016, **7**, 905–917.
45 S. Meloni, T. Moehl, W. Tress, M. Franckevičius, M. Saliba, Y. H. Lee, P. Gao, M. K. Nazeeruddin, S. M. Zakeeruddin, U. Rothlisberger and M. Graetzel, *Nat. Commun.*, 2016, **7**, 10334.
46 M. M. Tavakoli, P. Yadav, R. Tavakoli and J. Kong, *Adv. Energy Mater.*, 2018, **8**, 1800794.
47 Y. Dou, D. Wang, G. Li, Y. Liao, W. Sun, J. Wu and Z. Lan, *ACS Appl. Mater. Interfaces*, 2019, **11**, 32159–32168.
48 J. Peng, Y. Chen, K. Zheng, T. Pullerits and Z. Liang, *Chem. Soc. Rev.*, 2017, **46**, 5714–5729.
49 D. Shi, V. Adinolfi, R. Comin, M. Yuan, E. Alarousu, A. Buin, Y. Chen, S. Hoogland, A. Rothenberger, K. Katsiev, Y. Losovyj, X. Zhang, P. A. Dowben, O. F. Mohammed, E. H. Sargent and O. M. Bakr, *Science*, 2015, **347**, 519–522.
50 G.-J. A. H. Wetzelaer, M. Scheepers, A. M. Sempere, C. Momblona, J. Ávila and H. J. Bolink, *Adv. Mater.*, 2015, **27**, 1837–1841.
51 M. Nikolka, K. Broch, J. Armitage, D. Hanifi, P. J. Nowack, D. Venkateshvaran, A. Sadhanala, J. Saska, M. Mascal, S.-H. Jung, J. K. Lee, I. McCulloch, A. Salleo and H. Sirringhaus, *Nat. Commun.*, 2019, **10**, 2122.
52 D. Yang, X. Zhou, R. Yang, Z. Yang, W. Yu, X. Wang, C. Li, S. Liu and R. P. H. Chang, *Energy Environ. Sci.*, 2016, **9**, 3071–3078.
53 E. Aydin, M. De Bastiani and S. De Wolf, *Adv. Mater.*, 2019, **31**, 1900428.
54 J. Kim, A. Ho-Baillie and S. Huang, *Sol. RRL*, 2019, **3**, 1800302.

55 J. Luo, C. Jia, Z. Wan, F. Han, B. Zhao and R. Wang, *J. Power Sources*, 2017, **342**, 886–895.
56 H. Lai, B. Kan, T. Liu, N. Zheng, Z. Xie, T. Zhou, X. Wan, X. Zhang, Y. Liu and Y. Chen, *J. Am. Chem. Soc.*, 2018, **140**, 11639–11646.
57 W. Zhou, D. Li, Z. Xiao, Z. Wen, M. Zhang, W. Hu, X. Wu, M. Wang, W.-H. Zhang, Y. Lu, S. Yang and S. Yang, *Adv. Funct. Mater.*, 2019, **29**, 1901026.
58 W. Li, H. Dong, X. Guo, N. Li, J. Li, G. Niu and L. Wang, *J. Mater. Chem. A*, 2014, **2**, 20105–20111.
59 W. Li, H. Dong, L. Wang, N. Li, X. Guo, J. Li and Y. Qiu, *J. Mater. Chem. A*, 2014, **2**, 13587–13592.
60 J. C. Yu, D. B. Kim, G. Baek, B. R. Lee, E. D. Jung, S. Lee, J. H. Chu, D.-K. Lee, K. J. Choi, S. Cho and M. H. Song, *Adv. Mater.*, 2015, **27**, 3492–3500.
61 P. Luo, Y. Zhou, S. Zhou, Y. Lu, C. Xu, W. Xia and L. Sun, *Chem. Eng. J.*, 2018, **343**, 146–154.